Overspeeding characteristics of turbomachinery for gas generator cycle air turbo ramjet engine

Propulsion and Power Research 2022;11(4):444−456

http://ppr.buaa.edu.cn/

Propulsion and Power Research

www.sciencedirect.com

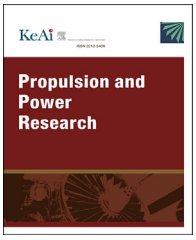

ORIGINAL ARTICLE

Overspeeding characteristics of turbomachinery for gas generator cycle air turbo ramjet engine

Ryojiro Minato[a,*], Daisuke Nakata[b], Masaharu Uchiumi[b], Ryoji Imai[a], Kazuyuki Higashino[b]

[a]*Department of Engineering, Muroran Institute of Technology Muroran, Hokkaido, 050-8585, Japan*
[b]*Aerospace Plane Research Center, Muroran Institute of Technology Muroran, Hokkaido, 050-8585, Japan*

Received 30 September 2021; accepted 23 October 2022
Available online 6 December 2022

KEYWORDS

Air turbo ramjet engine;
Compressor map;
Overspeeding;
Combustion efficiency

Abstract The main interest in the current study focuses on the possibility of overspeeding for the gas-generator cycle air turbo ramjet (GG-ATR) engine. The authors developed the air turbo ramjet engine and investigated its compressor performance. Based on those data, the authors developed the analytical code for the air turbo ramjet engine, which calculates the performances of turbomachinery, gas-generator, and ram combustor. The previous study described that the rotor overspeeding would not occur in the air turbo rocket engine. However, the current results show that degraded ram combustion can decrease the compressor pressure ratio and the compressor power. This reduced compressor power can cause overspeeding for the air turbo ramjet engine. The experimental results of compressor power and turbine inlet pressure support those analytical results.

*Corresponding author.
E-mail addresses: r-minato@mmm.muroran-it.ac.jp (Ryojiro Minato), nakata@mmm.muroran-it.ac.jp (Daisuke Nakata), uchiumi@mmm.muroran-it.ac.jp (Masaharu Uchiumi), r_imai@mmm.muroran-it.ac.jp (Ryoji Imai), k-higashino@msb.biglobe.ne.jp (Kazuyuki Higashino).

Peer review under responsibility of Propulsion and Power Research.

ELSEVIER Production and Hosting by Elsevier on behalf of KeAi

1. Introduction

An air turborocket or air turbo ramjet (ATR) engine is a type of turbine-based combined cycle (TBCC) engine. It can be a candidate for a propulsion engine of a hypersonic vehicle or a spaceplane [1−8]. The ATR engine has a greater specific thrust than turbojet engines and a higher specific impulse (Isp) than rocket engines. Kobayashi et al. consider the ATR engine

https://doi.org/10.1016/j.jppr.2022.10.001

Nomenclature

A	cross section area (unit: m^2)
C^*	characteristic velocity as represent in Eq. (4) (unit: m/s)
C_0	spouting velocity at the turbine nozzle
C_P	heat capacity at constant pressure (unit: J/(kg·K))
$d_{1,k}$, $d_{2,k}$, $d_{3,k}$	polynomial coefficients for turbine module in Eq. (10)
M	Mach number
$\dot{M}_{cor}$	corrected mass flow rate as function of $\pi_{comp,i}$ (unit: kg/s)
m	mass flow rate (unit: kg/s)
N	rotational speed (unit: rpm)
P	pressure (unit: Pa)
R	gas constant (unit: J/(kg·K))
T	temperature (unit: K)
U	rotational speed of turbine blade (unit: m/s)
V	velocity (unit: m/s)
w	specific power of compressor or turbine (unit: W)

Greek letters

η	efficiency
H_s	adiabatic compression efficiency as function of m_{cor}
κ	specific heat capacity ratio
Π_s	total-to-static compressor pressure ratio as function of $\dot{m}_{cor,i}$
π	pressure ratio at engine component
ρ	density (unit: kg/m^3)
τ	temperature ratio at engine component

Subscript

air	airflow
cho	choke condition
comp	compressor
cor	corrected value
de	on design condition
fuel	fuel
GG	gas generator
i	index for the referential corrected rotation speed
ideal	ideal condition
in	inlet condition
k	degree of polynomial
nozzle	turbine nozzle
out	outlet condition
ram	ram combustor
ref	referential condition
s	static condition
spout	gas spouting at turbine nozzle
sur	surge condition
T	stagnation condition
turb	turbine
0	ambient condition
1	air intake inlet
2	compressor inlet
3	compressor outlet
4	turbine inlet
5	turbine outlet
6	ram combustor inlet
7	ram combustor outlet
8	nozzle throat
9	exit of nozzle

for the reusable launch vehicle due to those advantages [9]. As well as Ref. [9], the authors also have developed the ATR engine for the supersonic unmanned aerial vehicle [10], including the propellant feeding system [11,12]. Unlike a turbojet engine, the propellant gas of the ATR engine drives its turbine. For a gas-generator cycle air turbo ramjet (GG-ATR) engine, fuel and oxidizer are burned at the gas generator (GG) in fuel-rich conditions. The GG combustion provides the enthalpy for turbine power. The fuel-rich turbine effluent gas burns with air from the compressor in the downstream ram combustor. Previous studies have investigated various liquid propellants [6−8] and solid propellants [13−15] for the GG-ATR engine. Figures 1 and 2 show the ATR engine developed at Muroran Institute of Technology and its conceptual schematic, respectively. The authors conducted the GG-ATR engine turbomachinery tests, which employed nitrogen gas (GN_2) or helium gas as turbine driving gas instead of GG combustion gas. In an actual GG-ATR engine operation, a nozzle throat plays a role in controlling the ram combustor pressure and the gas flow rate. However, the authors do not still develop the ram combustor. Thus, the authors install the orifice at the compressor exit to control the airflow rate in the tests. Replacing the orifices changes the compressor operating condition to obtain the compressor characteristic map data.

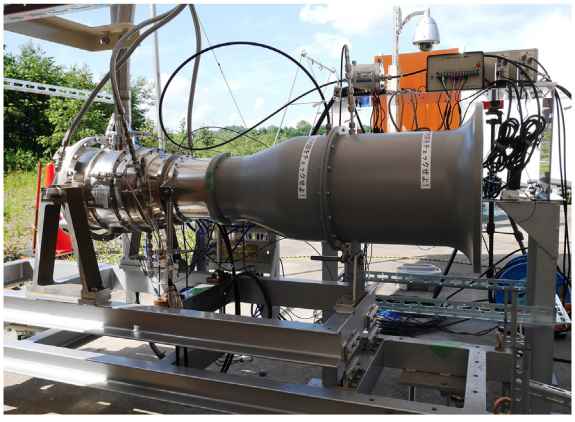

Figure 1 GG-ATR engine on the test bed.

The turbomachinery characteristics of the GG-ATR engine differ from a turbojet engine. The source of turbine power for the GG-ATR engine comes from GG combustion gas. The compressor power at the high altitude will be lower than the sea-level static conditions because the air density is lower at the high altitude. Thus, propellant flow rates should be strictly controlled to keep the rotor speed constant. Otherwise, overspeeding will occur. The

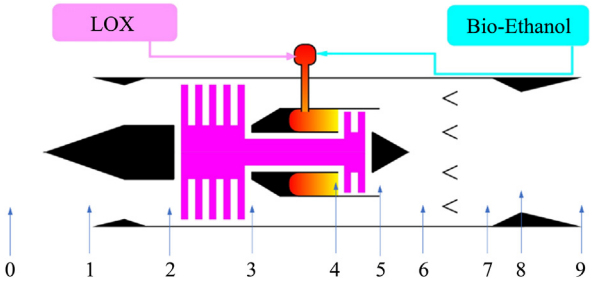

Figure 2 Conceptual schematic of GG-ATR engine [6,7].

propellant flow rate control is subject to the GG-ATR engine characteristics, such as a compressor, turbine, and gas generator. Many researchers have investigated the GG-ATR engine component characteristics so far. In contrast, Lilly et al. carried out the engine component integration and the GG-ATR tests [16]. For engine component studies, Refs. [13,14] discussed the gas generator and ram combustor performances. Liu et al. proposed the matching model of an intake-compressor interaction for the GG-ATR engine and numerically assessed its viability [17]. Bussi et al. investigated the off-design performance of the GG-ATR compressor [18,19]. Bossard and Thomas focused on the surge/stall phenomena of the GG-ATR engine compressor [20]. They concluded that the GG-ATR engine did not have the possibility of overspeeding because the gas generator fully controls the shaft power to the compressor. However, the choke flow at the nozzle throat depends on the mass flow rate, total pressure, and total temperature. Thus, it can affect the compressor pressure ratio/airflow rate characteristics. The overspeeding discussion in Ref. [20] did not include the ram combustor performance, i.e., combustion efficiency. Low ram combustion efficiency decreases the total temperature at the nozzle throat, which affect the compressor operation condition. This situation can vary the compressor power and might increase the rotational speed of the rotor.

The turbine power of the GG-ATR engine is independent of its compressor operation. It means the GG-ATR engine has the potential to overspeeding. Thus, the actual GG-ATR engine operation necessitates the appropriate model to predict its overspeeding. This model should consider the interaction between the turbomachinery and the ram combustor. Therefore, the objective of the current study is to develop the GG-ATR engine analytical model and evaluate the overspeeding risk of the GG-ATR engine. The authors conducted the GG-ATR engine test and its CFD analysis. Based on those results, the new analytical code is developed for the GG-ATR engine performance prediction. This code analyzes all engine components, such as turbomachinery, gas-generator, and ram combustor. Its code validation is carried out by using the GG-ATR engine test data.

2. GG-ATR engine and experimental facility

2.1. Specification of GG-ATR engine

Table 1 lists the specifications of the GG-ATR engine at Muroran Institute of Technology. This GG-ATR engine uses liquefied oxygen (LOX) and ethanol as an oxidizer and a fuel, respectively. LOX and ethanol are injected into the gas generator and burned to generate the turbine-driving gas. Figures 3 and 4 show the rotor element and the mixed flow compressor configuration of the GG-ATR engine, respectively. The rotor impeller of this mixed flow compressor is made of titanium alloy (Ti-6Al-4V). It has seven main blades and seven splitters in the rotor. The diffuser has eight stator blades. The tip diameters of the mixed flow compressor impeller are 150 mm and 167.2 mm at the inlet and outlet, respectively. The outer and inner diameters at the diffuser exit are 210 mm and 144 mm, respectively. In the on-design condition, the rotational speed is 58,000 rpm, which corresponds to 507 m/s of the circumferential tip speed. The airflow rate of this mixed flow compressor is 3.47 kg/s, and the total-to-static pressure ratio is 2.27.

The turbine of the GG-ATR engine is a two-staged axial one, as shown in Figure 3. The turbine blisks are made of nickel-based alloy (INCONEL 713). The turbine inlet pressure is 1.35 MPa, and the total-to-static turbine expansion ratio is about 6. The turbine inlet temperature is strictly limited to 1100 K due to the thermal limit of a turbine blade. The pitch diameter of the turbine blade is 95 mm. Thus, the rotational speed of the turbine blade is up to 288.5 m/s at the on-design condition.

2.2. Experimental facility

The authors carried out the GG-ATR engine turbomachinery tests using nitrogen (GN_2) or helium gas (GHe) as turbine driving gas. The authors utilized three gas cylinder

Table 1 GG-ATR engine specification.

Rotational speed at design point	58,000 rpm
Compressor inlet diameter	150 mm
Maximum diameter	231 mm
Pressure ratio of compressor (total-to-static)	2.27
Adiabatic compression efficiency (total-to-static)	70.2%
Air flow rate	3.47 kg/s
GG combustion temperature	1100 K
GG combustion pressure	1.35 MPa
Mass flow rate of GG combustion gas	0.7 kg/s
Expansion ratio at turbine (total-to-static)	6
Adiabatic turbine efficiency (total-to-static)	65%
Ram combustor temperature	2380 K
Thrust at sea level static condition	3804 N
Isp at sea level static condition	555.4 s

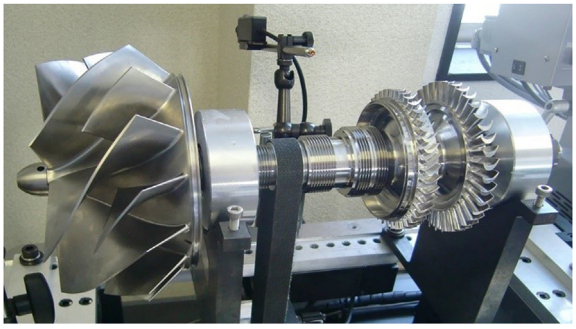

Figure 3 Rotor element of GG-ATR engine.

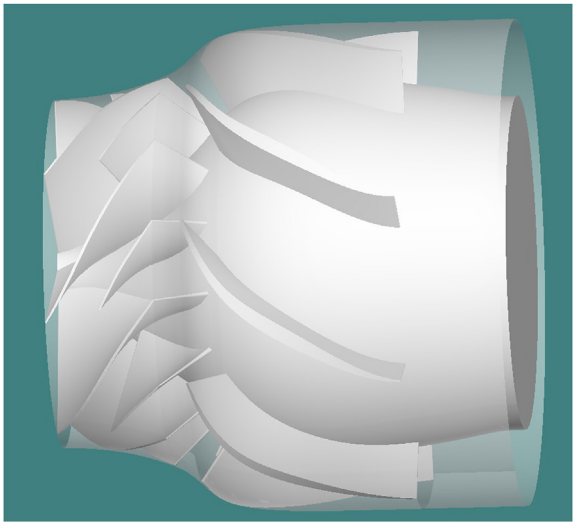

Figure 4 Mixed flow compressor of GG-ATR engine.

bundles (1 bundle has 20 gas cylinders for N_2 gas and 25 for helium gas) and connected them to this test facility. GN_2 is supplied from those bundles to the turbine manifold of the GG-ATR engine and drives the turbine. The temperature of GN_2 in gas cylinder bundles is equal to room temperature, which is much lower than GG combustion gas. Thus, the turbine power for GN_2 is lower than that for GG combustion gas, and the maximum rotational speed of the turbine is limited to 42,000 rpm for the turbine driving gas of GN_2. It is about 70% of the rated rotational speed (58,000 rpm). Therefore, helium gas must be used as the turbine driving gas at the rated rotational speed. The maximum GN_2 flow rate is 2.0 kg/s with total pressure at the turbine manifold of 1.6 MPa. That of GHe is 0.58 kg/s with total pressure at the turbine manifold of 0.85 MPa.

In the GN_2 or GHe supplying tube of this facility, the authors employed the orifice plate flow meter to measure the mass flow rate of GN_2 or GHe. The thermocouple and the pressure transducer measure the temperature and static pressure upstream of the orifice, respectively. Moreover, the differential pressure across the orifice also is acquired by the pressure transducer. The bell mouth is installed on the compressor inlet to rectify the airflow rate. The orifice plate is installed in the bell mouth to measure the airflow rate. The discharge coefficients for both orifice plate flow meters are cited in Ref. [21]. The authors carried out the pressure and temperature measurements at each engine component. Those data evaluate the compressor pressure ratio, turbine expansion ratio, and adiabatic compressor and turbine efficiencies.

3. CFD analysis for turbomachinery

The authors conducted CFD analysis to evaluate the turbomachinery performance of the GG-ATR engine in the present study. The authors employ the commercial software Fine TURBO$^{@}$ by Numeca INTERNATIONAL Inc. for CFD analysis. The governing equation is the three-dimensional turbulent Navier Stokes equation with the Spalart-Allmaras 1-equation turbulence model. The rotational speed is ranged from 50% to 110% of the rated speed. The air in the CFD model is treated as calorically perfect gas because the temperature in the numerical solution does not exceed 450 K. On the other hand, the turbine analysis treats the GG combustion gas as the thermally perfect gas. To generate the numerical grid, the authors employ Auto Grid$^{@}$, presented by Numeca INTERNATIONAL Inc. The average y^+ on the wall boundary is about 1.0. The authors use the mixing plane condition to model the interface between stator and rotor because of its simplicity.

The total temperature and pressure at the inlet boundary for the compressor analysis are given as 288.15 K and 101.3 kPa, respectively. The total pressure at the turbine inlet depends on the compressor power, as described in the next section. The total temperature at there is determined under constant O/F condition and has the pressure dependency. The total temperature and the total pressure at the turbine inlet boundary for the rated rotational speed are 1100 K and 1350 kPaA, respectively. In the off-design condition, those ranges from 1024 K to 1111 K and from 400 kPaA to 1600 kPaA for total temperature and pressure, respectively.

Four numerical grids are tested in the grid independence tests for the compressor and turbine analyses. The grid point numbers are 1.22, 2.14, 4.08, and 5.92 million for the compressor analysis, and those are 1.08, 2.13, 4.21, and 6.36 million for turbine ones. Figure 5(a) indicates the result of the grid independence test for the compressor analysis, which shows the compressor characteristic map at 70% of the rated rotational speed. The numerical results of those four grids are almost identical to each other. However, only a 1.22 million grid has a slight higher pressure ratio than other three grids near the surge condition. Therefore, 2.14 million grid is employed in the present study.

Figure 5(b) shows the grid dependence test for the turbine analysis. The maximum difference in adiabatic turbine efficiency is 0.9% among 2.12, 4.21, and 6.36 million grids. However, the difference between 1.08 million and 6.36 million grids is nearly equal to 2.0%. Therefore, 2.12 million grid is employed for the turbine analysis.

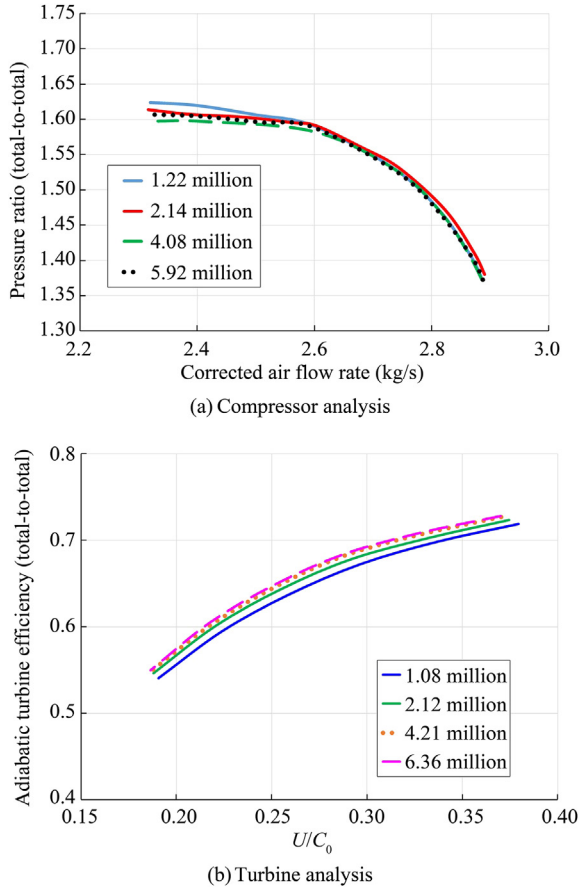

Figure 5 Grid dependence tests. (a) Compressor analysis, (b) turbine analysis.

Figure 6 shows one example of the present CFD results, which is the total pressure distribution of the present mixed flow compressor in the on-design condition.

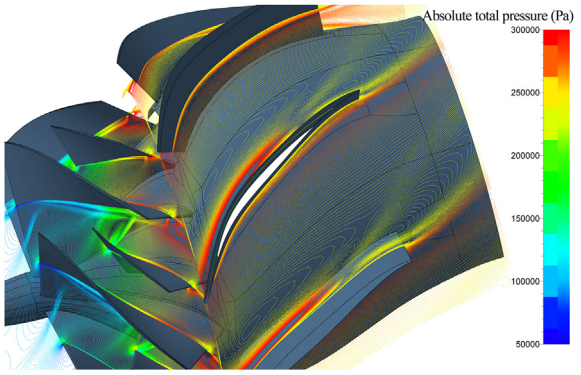

Figure 6 Total pressure distribution of the present mixed flow compressor in on-design condition.

code for the detailed GG-ATR engine analysis. The GG-ATR engine operation has two operating constraints, A) compressor-turbine power balance and B) nozzle choke condition. Equation (1) represents constraint A).

$$\frac{\dot{m}_{air} C_P T_{T2}}{\eta_{comp}} \left(\pi_{comp}^{\frac{\kappa-1}{\kappa}} - 1 \right) = \eta_{turb} \dot{m}_{GG} C_{P,GG} T_{GG} \left(1 - \left(\frac{P_{T5}}{P_{GG}} \right)^{\frac{\kappa_{GG}-1}{\kappa_{GG}}} \right) \tag{1}$$

Equation (2a) corresponds to the constraint B) in choked flow condition.

$$\dot{m}_{air} + \dot{m}_{GG} = P_{T7} A_8 \sqrt{\frac{\kappa_{ram}}{R_{ram} T_{T7}} \left(\frac{2}{\kappa_{ram}+1} \right)^{\frac{\kappa_{ram}+1}{\kappa_{ram}-1}}} \tag{2a}$$

On the other hand, Eq. (2b) indicates the constraint B) in unchoked flow condition.

$$\begin{aligned} \dot{m}_{air} + \dot{m}_{GG} &= P_{T7} A_8 \sqrt{\frac{2\kappa_{ram}}{(\kappa_{ram}-1) R_{ram} T_{T7}} \left(\left(\frac{P_{T7}}{P_0} \right)^{-\frac{2}{\kappa_{ram}}} - \left(\frac{P_{T7}}{P_0} \right)^{-\frac{\kappa_{ram}+1}{\kappa_{ram}}} \right)} \\ &= P_0 A_8 \sqrt{\frac{2\kappa_{ram}}{(\kappa_{ram}-1) R_{ram} T_{T7}} \left(\left(\frac{P_{T7}}{P_0} \right)^{\frac{2(\kappa_{ram}-1)}{\kappa_{ram}}} - \left(\frac{P_{T7}}{P_0} \right)^{\frac{\kappa_{ram}-1}{\kappa_{ram}}} \right)} \end{aligned} \tag{2b}$$

4. GG-ATR engine cycle analysis

4.1. Engine system and operational constraints

The prediction of a GG-ATR engine operating state is indispensable for its development and requires its cycle analysis. The cycle analysis of a GG-ATR engine is quite different from that of a turbojet engine. Thus, the authors developed the GG-ATR engine cycle analysis (GATRECA)

where P_{T5} and P_{T7} are the total pressure at the turbine and the ram combustor outlet, respectively.

In Eq. (1), the compressor operating state is described by air flow rate, m_{air}, compressor pressure ratio, π_{comp} (total-to-total), and adiabatic compression efficiency, η_{comp} (total-to-total). On the other hand, GG gas flow rate, m_{GG}, GG combustion temperature, T_{GG}, and GG combustion pressure, P_{GG}, are variables concerned with GG combustion. The chemical equilibrium calculation can determine T_{GG} under a

given P_{GG} and oxidizer-to-fuel (O/F) ratio. GG combustion gas flow is always choked at the turbine nozzle. Thus, the following Eq. (3) can hold for the m_{GG}-P_{GG} relationship.

$$\dot{m}_{GG} = \frac{P_{GG}\, A_{nozzle}}{C^*_{GG}} \tag{3}$$

where A_{nozzle} is the cross-section area at the turbine nozzle. C^*_{GG} is the characteristic velocity at the GG and is represented in Eq. (4).

$$C^*_{GG} = \sqrt{\frac{R_{GG}\, T_{GG}}{\kappa_{GG}} \left(\frac{\kappa_{GG}+1}{2}\right)^{\frac{\kappa_{GG}+1}{\kappa_{GG}-1}}} \tag{4}$$

The variables related to the compressor and GG combustion must satisfy Eqs. (1) and (2) concurrently. Thus, the GATRECA code treats π_{comp} and P_{GG} as the independent variables and determines them by solving Eqs. (1) and (2). However, those equations have non-linearity, and some root-finding algorithms are necessary, such as Newton-Raphson method. P_{T5}, P_{T7}, and m_{air} are the dependent variables of π_{comp}. On the other hand, m_{GG} and T_{GG} are those of P_{GG}.

The GATRECA code contains some engine component modules and evaluates each component's performance, such as turbomachinery, gas-generator, and ram combustor. Subsections 4.2 to 4.5 describe the analytical model for those engine components, and subsection 4.6 treats the engine cycle analysis procedure.

4.2. Compressor analysis

The compressor operation analysis requires a mathematical model for a compressor map. Reference [22] describes the simplified exponential model for compressor characteristics. This model employs the exponential approximation and requires defining three compressor operating states, i.e., the stall-surge line, the operating line, and the choke condition. The choke condition means the low-pressure side of the pressure ratio-airflow rate curve in the compressor map. The pressure ratio in the choke condition does not have a particular physical meaning. However, it is necessary to set up the present model. Unfortunately, this simplified exponential model is not necessarily accurate in describing the compressor behaviors because it identifies only three points to draw one pressure ratio-airflow rate curve.

The authors present the following approximation model for a more accurate prediction of the compressor operation. This model assigns several referential rotational speeds in advance. Those referential rotational speeds are from 70% to 110% of the rated speed with a 5% interval. Besides those, 50% and 60% of the rated speed are added to the referential speeds. The authors conducted CFD analysis for those referential speeds to evaluate the compressor performance. The corrected rotational speed, N_{cor}, and the Total-to-total compressor pressure ratio, π_{comp}, at the arbitrary operating point are the input data in the compressor module. N_{cor} is assumed to be between the ith and $(i+1)$th referential rotational speeds (donated as $N_{ref,i}$ and $N_{ref,i+1}$, respectively). $\pi_{comp,i}$ and $\pi_{comp,i+1}$ are the total-to-total compressor pressure ratios at $N_{ref,i}$ and $N_{ref,i+1}$, respectively. Those correlations are described in Eq. (5) by Ref. [23].

$$\begin{aligned}
\pi_{comp,i} &= \left(1 + \left(\frac{N_{ref,i}}{N_{cor}}\right)^2 \left(\pi_{comp}^{\frac{\kappa-1}{\kappa}} - 1\right)\right)^{\frac{\kappa}{\kappa-1}} \\
\pi_{comp,i+1} &= \left(1 + \left(\frac{N_{ref,i+1}}{N_{cor}}\right)^2 \left(\pi_{comp}^{\frac{\kappa-1}{\kappa}} - 1\right)\right)^{\frac{\kappa}{\kappa-1}}
\end{aligned} \tag{5}$$

Figure 7 indicates the correlation of Eq. (5). On the constant $N_{ref,i}$ operating line, specifying compressor pressure ratio can determine the corrected airflow rate. The corrected airflow rate, $m_{cor,i}$, is given as a function of $\pi_{comp,i}$ in Eq. (6).

$$\dot{m}_{cor,i} = \dot{M}_{cor}(\pi_{comp,i}) \tag{6}$$

$$\pi_{s,comp,i} = \Pi_s(\dot{m}_{cor,i}) \tag{7}$$

$$\eta_{s,comp,i} = H_s(\dot{m}_{cor,i}) \tag{8}$$

The total-to-static pressure ratio of the compressor, $\pi_{s,comp,i}$, and the adiabatic compression efficiency, $\eta_{s,comp,i}$, are given as functions of $m_{cor,i}$ in Eqs. (7) and (8), respectively. Functions from Eqs. (6)−(8) algebraically approximate the relationships among $m_{cor,i}$, $\pi_{s,comp,i}$, $\eta_{s,comp,i}$, and π_{comp}. Those equations are established along the constant $N_{ref,i}$ line.

Finally, the following linear interpolations give the corrected airflow rate, m_{cor}, compressor pressure ratio (total-to-static), $\pi_{s,comp}$, and the adiabatic compression efficiency (total-to-static), $\eta_{s,comp}$, at the operating point.

$$\begin{aligned}
\dot{m}_{cor} &= \dot{m}_{cor,i} + \overline{N}_{cor}(\dot{m}_{cor,i+1} - \dot{m}_{cor,i}) \\
\pi_{s,comp} &= \pi_{s,comp,i} + \overline{N}_{cor}(\pi_{s,comp,i+1} - \pi_{s,comp,i}) \\
\eta_{s,comp} &= \eta_{s,comp,i} + \overline{N}_{cor}(\eta_{s,comp,i+1} - \eta_{s,comp,i}) \\
\overline{N}_{cor} &= \frac{N_{cor} - N_{ref,i}}{N_{ref,i+1} - N_{ref,i}}
\end{aligned} \tag{9}$$

m_{cor}, $\pi_{s,comp}$, and $\eta_{s,comp}$ can determine the total temperature at the compressor exit, T_{T3}, the total-to-total adiabatic compression efficiency, η_{comp}, and the specific compression power, w_{comp}. Figure 8 indicates the validation of the present methods in the GATRECA code with CFD analytical results. The analytical results in the GATRECA code agree well with the CFD results of compressor performance.

4.3. Turbine analysis

The present subsection describes the analytical procedure in the turbine module. The input data for the turbine module

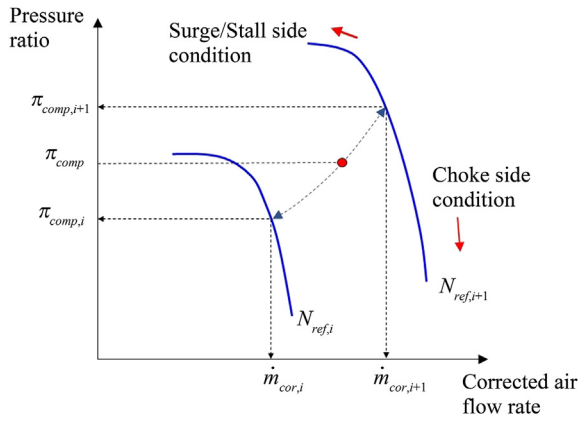

Figure 7 Concepts of Eq. (5) on compressor map.

are the rotational speed, N, static pressure at the turbine exit, P_{s5}, GG combustion pressure, P_{GG}, and temperature, T_{GG}. P_{s5} is equal to the static pressure at the compressor exit, P_{s3}. P_{GG} and T_{GG} correspond to turbine inlet pressure and temperature, respectively. The pressure ratio of P_{GG}/P_{s5} is defined as the total-to-static turbine expansion ratio, $\pi_{s,turb}$. The present turbine analysis employs the following three polynomial correlations.

$$\begin{aligned}\pi_{turb} &= \sum_{k=0}^{4} d_{1,k}(\pi_{s,turb})^k \\ M_{spout} &= \sum_{k=0}^{4} d_{2,k}(\pi_{turb})^k \\ \eta_{turb} &= \sum_{k=0}^{4} d_{3,k}(U/C_0)^k\end{aligned} \tag{10}$$

The first formula in Eq. (10) is the polynomial of the total-to-total turbine expansion ratio, π_{turb} as a function of $\pi_{s,turb}$. The total pressure at the turbine outlet, P_{T5}, is equal to the product of P_{GG} and π_{turb}. Reference [24] describes that the adiabatic turbine efficiency is given as a function of the ratio of the pitch-line rotor velocity, U, to theoretical gas spouting velocity, C_0. U is linearly proportional to the rotational speed. C_0 is represented as the product of the gas

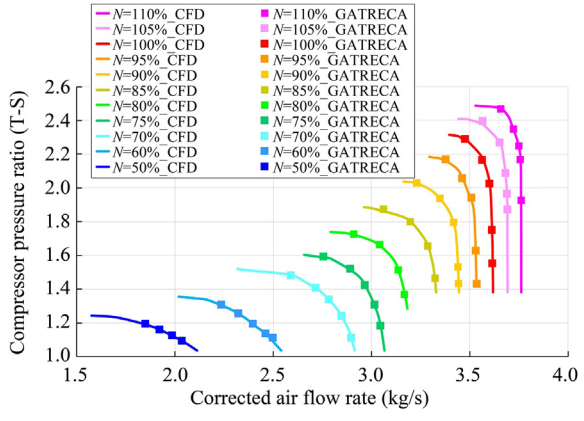

Figure 8 Comparison between CFD and GATRECA code.

spouting Mach number, M_{spout}, and its sonic speed. M_{spout} is approximated as the polynomial of the pressure ratio of π_{turb}. The second formula represents this relationship between M_{spout} and π_{turb}. Finally, the third formula is the polynomial of the adiabatic turbine efficiency, η_{turb}, as a function of velocity ratio, U/C_0. With those three formulas, η_{turb} can be calculated from $\pi_{s,turb}$. The authors utilize the CFD results to determine those polynomial coefficients in Eq. (10).

The total temperature at the turbine exit, T_{T5}, can be calculated from T_{GG}, π_{turb}, and η_{turb}. Those results can determine the specific turbine power, w_{turb}. The authors consider that the turbine expansion is a chemical frozen process because the turbine power in the chemical frozen condition is identical to that in the chemical equilibrium condition [25]. In the turbine module, η_{turb}, w_{turb}, P_{T5}, and T_{T5}, are its output data.

4.4. Gas generator analysis

The objective of the GG module is to specify the oxidizer-to-fuel ratio for a given GG combustion condition. The GG module assigns the combustion temperature, pressure, and type of fuel/oxidizer as the input data. The O/F ratio is the output data of the GG module.

In the gas generator (GG) module, the GG combustion temperature and pressure are specified in the On-design condition in advance. The O/F ratio is determined in the GG module to achieve a given combustion temperature. This O/F ratio is always constant, even if the engine operating states change. The GG module contains the chemical equilibrium calculation to evaluate the combustion temperature and the gas species. The authors developed the computation code for the chemical equilibrium calculation and thoroughly verified its accuracy compared to the computation of NASA-CEA [26].

4.5. Ram combustor and nozzle analyses

This subsection describes the analytical procedure in the ram combustor and the nozzle modules. A ram combustor is an element where the fuel-rich GG combustion gas burns with the air discharged from the compressor. Rayleigh flow theory treats a flow in a duct with heating or cooling, such as the ram combustor flow, and can evaluate the pressure recovery there [27]. Rayleigh's flow theory builds on mass conservation and momentum conservation laws.

$$\dot{m}_{ram} = \dot{m}_{air} + \dot{m}_{GG} \tag{11}$$

$$P_{s7}A_7\left(1+\kappa_{ram}M_7^2\right) = P_{s3}A_3\left(1+\kappa M_3^2\right) + P_{s5}A_5\left(1+\kappa_{GG}M_5^2\right) \tag{12}$$

The mass flow rate at the ram combustor in Eq. (11) can be represented by using static pressure, P_{s7}, and Mach number, M_7.

$$\dot{m}_{ram} = \rho_7 V_7 A_7 = P_{s7} A_7 M_7 \sqrt{\frac{\kappa_{ram}}{R_{ram} T_{T7}} \left(1 + \frac{\kappa_{ram} - 1}{2} M_7^2\right)} \quad (13)$$

Eq. (14) can be obtained from Eq. (13).

$$\frac{\dot{m}_{ram}}{P_{s7} A_7} \sqrt{\frac{R_{ram} T_{T7}}{\kappa_{ram}}} = M_7 \sqrt{1 + \frac{\kappa_{ram} - 1}{2} M_7^2} \quad (14)$$

The static pressure at the compressor exit is equal to the turbine exit static pressure, which is the same as that at the ram combustor inlet. The compressor-turbine power balance in Eq. (1) can determine the mixture ratio of the GG combustion gas to the air. The chemical equilibrium calculation can determine the theoretical total temperature at the ram combustor, $T_{T7,ideal}$, under a given mixture ratio of m_{GG}/m_{air} and the pressure of P_{T3}. The effect of the pressure difference between P_{T3} and P_{T7} on T_{T7} is negligible. Considering the ram combustor efficiency, the total temperature at the ram combustor, T_{T7}, is given in Eq. (15).

$$T_{T7} = T_{T7,ideal} \eta_{ram}^2 \quad (15)$$

The definition of ram combustion efficiency is described later. The momentum conservation law in Eq. (12) gives the static pressure ratio, P_{s7}/P_{s3}.

$$\frac{P_{s7}}{P_{s3}} = \frac{A_3\left(1 + \kappa M_3^2\right) + A_5\left(1 + \kappa_{GG} M_5^2\right)}{A_7\left(1 + \kappa_{ram} M_7^2\right)} \quad (16)$$

M_3 and M_5 are Mach numbers at the exit of the compressor and the turbine, respectively, and are known quantities. The unknown variables in Eqs. (14) and (16) are the Mach number at the ram combustor exit, M_7, and P_{s7}. Equations (14) and (16) are the dual simultaneous equation. Using Eq. (16) and eliminating the variable $P_{s7}A_7$ from Eq. (14), it can be solved as a quadric equation of M_7^2. M_7 and P_{s7} can determine the total pressure at the ram combustor exit, P_{T7}.

The GATRECA code in the nozzle module evaluates the nozzle performance based on the compressible gas dynamics theory. Equation (17) can give the static pressure at the nozzle exit and the exhaust gas velocity. In some cases, shock waves may be present in the divergent nozzle. The actual calculation in the nozzle module considers the effect of the shock wave.

$$\frac{A_9}{A_8} = \frac{1}{M_9}\left(\frac{2 + (\kappa_{ram} - 1)M_9^2}{\kappa_{ram} + 1}\right)^{\frac{\kappa_{ram}+1}{2(\kappa_{ram}-1)}}$$
$$\frac{P_{T9}}{P_{s9}} = \left(1 + \frac{\kappa_{ram} - 1}{2} M_9^2\right)^{\frac{\kappa_{ram}}{\kappa_{ram}-1}} \quad (17)$$
$$V_9 = \sqrt{\frac{2\kappa_{ram}}{\kappa_{ram} - 1} R_{ram} T_{T9} \left(1 - \left(\frac{P_{s9}}{P_{T9}}\right)^{\frac{\kappa_{ram}-1}{\kappa_{ram}}}\right)}$$

One of the most significant factors in determining the GG-ATR engine operating state is to estimate the cross-sectional area at the nozzle throat, A_8, in Eq. (2). As indicated in Eq. (2), A_8 affects $m_{air}+m_{GG}$, P_{T7}, and T_{T7}. T_{T7} strongly depends on the combustion efficiency at the ram combustor. Thus, the actual design of the nozzle throat requires an accurate estimation of the combustion efficiency. The combustion performance of a rocket engine is usually evaluated by C^* efficiency, which is the ratio of the actual characteristic velocity to the ideal one. C^* efficiency is valid for the ram combustor efficiency evaluation in a choked nozzle flow. However, it is not for an unchoked nozzle flow. Therefore, Eqs. (2a) and (2b) derive the following Eq. (18). The term on the left-hand side is proportional to the square root of T_{T7}, whether the nozzle flow is choked or not.

$$\frac{P_{T7} A_8}{\dot{m}_{air} + \dot{m}_{GG}} \propto \sqrt{T_{T7}} \quad (18)$$

The ram combustion efficiency is defined as the square root of temperature ratio of T_{T7} and $T_{T7,ideal}$.

$$\eta_{ram} = \sqrt{\frac{T_{T7}}{T_{T7,ideal}}} \quad (19)$$

where $T_{T7,ideal}$ is the theoretical ram combustor temperature. As well as T_{GG}, the chemical equilibrium calculation can evaluate $T_{T7,ideal}$ under a given P_{T7} and m_{GG}/m_{air} ratio. The authors define the referential ram combustion efficiency, η_{ram}, to determine the cross-sectional area, A_8, from Eq. (2). In the present study, the referential η_{ram} is set to 100%, which means that A_8 is determined under the ram combustor temperature of $T_{T7,ideal}$.

The combustion process in the GG-ATR engine ram combustor is more like a turbojet engine afterburner instead of a rocket engine. The combustion efficiency at an afterburner is defined as the ratio of the actual temperature rise to the ideal one [19]. In the present study, η_{ram} is ranged from 82% to 100%, which means the minimum T_{T7} is identical to two-thirds of $T_{T7,ideal}$. η_{ram} of 82% in Eq. (19) corresponds to 58% of combustion efficiency defined in Ref. [28]. This value of combustion efficiency is close to the minimum afterburner combustion efficiency. Therefore, this assumption gives a reasonable range for the ram combustion efficiency.

4.6. Sequence of analytical procedure

The GG-ATR engine cycle analysis (GATRECA) code integrates those engine component modules and solves the two constraints in Eqs. (1) and (2). The computational procedure of the GATREAC code is listed below.

1) At first, the rotational speed of the rotor, N, the ambient pressure, P_0, and temperature, T_0, are specified. The present study assumes the sea-level static conditions.

Thus, the ambient pressure and temperature are 101.3 kPa and 288.15 K, respectively.

2) The total pressure, P_{T2}, and temperature, T_{T2}, at the intake outlet are calculated by considering the intake performance. The corrected air flow rate and the corrected rotational speed are calculated with P_{T2} and T_{T2}.
3) Set the assumed values for P_{GG} and π_{comp}. Those are the independent variables in the iterative procedure.
4) The compressor and the GG modules evaluate their performances by using P_{GG}, π_{comp}, the corrected air flow rate, m_{cor}, and the corrected rotational speed, N_{cor}. The turbine module uses the static pressure at the compressor outlet, P_{s3}. The GG modules provides T_{GG} to the turbine module.
5) The ram combustor module conducts the chemical equilibrium calculation to determine its combustion temperature, gas species, and pressure recovery by using the results in the compressor and the turbine modules.
6) The output data from each engine components module can evaluate the errors in the constraint of Eqs. (1) and (2). The modification of the assumed values of P_{GG} and π_{comp} is determined by Newton-Raphson method. The computation goes back to 3) to repeat if those errors do not converge less than a certain level.

Figure 9 indicates the flow chart of GATRECA computation. The exhaust gas velocity, V_9, is obtained at the end of the flow chart. V_9 can determine the propulsive performance of the GG-ATR engine.

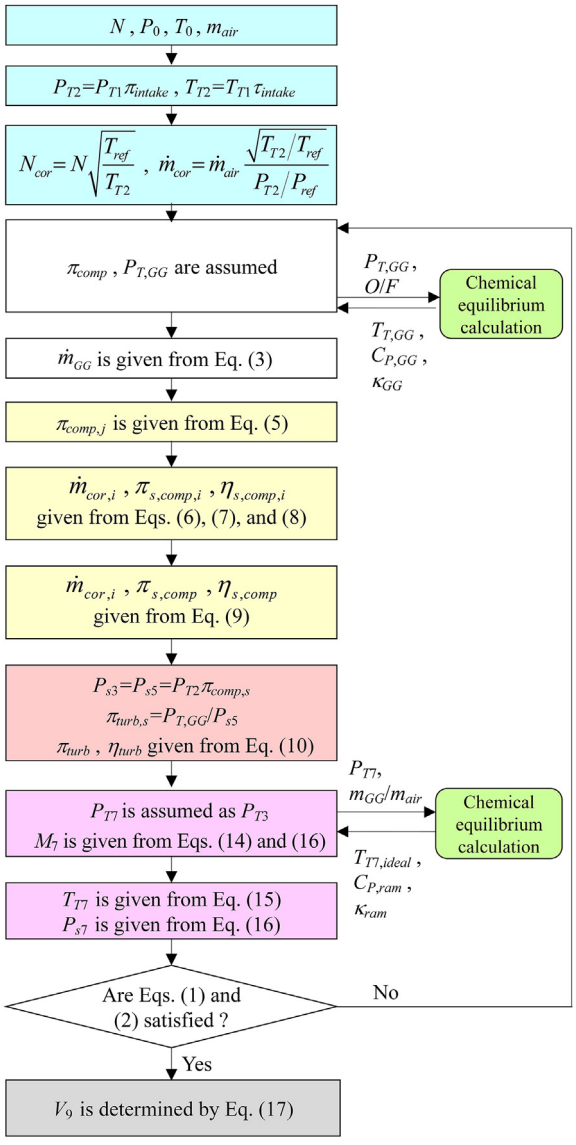

Figure 9 Flow chart of GATRECA computation.

5. Results and discussion

5.1. Experimental and analytical compressor performance

The authors have investigated the mixed-flow compressor performance for the GG-ATR engine in the turbomachinery tests. Figures 10 and 11 indicate the characteristic map for this compressor. The compressor pressure ratio in Figures 10 and 11 are evaluated as total-to-static and total-to-total ones, respectively. The authors experimentally measured the static pressure, P_{s3}, and total temperature at the compressor exit, T_{T3}, to evaluate the compressor performance. With Eq. (20), the authors calculated the airflow Mach number at the compressor exit, M_3, and determined the total pressure at the compressor exit, P_{T3}.

$$\dot{m}_{air} = P_{s3}A_3M_3\sqrt{\frac{\kappa}{RT_{T3}}\left(1+\frac{\kappa-1}{2}M_3^2\right)} \tag{20}$$

where A_3 is the cross-section area at the compressor exit. The total pressure at the compressor exit, P_{T3}. The total-to-total pressure ratio, π_{comp}, can be evaluated by using P_{T3}.

The solid lines in Figures 10 and 11 indicate the CFD results, and the dots do the experimental data. The error bar indicates the measurement error in those figures. Up to 70% of the corrected rotational speed, N_{cor}, GN_2 is used as turbine driving gas, and GHe is done for tests in higher N_{cor} conditions. The GG-ATR engine turbomachinery tests require a large amount of helium gas to drive at the rated rotational speed (N_{cor} = 100%). Unfortunately, helium gas is very costly, and the opportunities are strictly limited to testing in higher N_{cor} conditions. A limited number of tests are possible to use GHe as turbine driving gas. However, CFD results agree well with the experimental data in both Figures 10 and 11.

It should be noted that the actual compressor operation might encounter not only surge/stall but also other unsteady phenomena, such as supersonic unstalled flutter [29]. The flutter prediction requires the aeroelastic analysis of the compressor blades. Fortunately, the present mixed flow compressor tests did not observe such unsteady phenomena. Thus, the engine cycle analysis in the following section does not deal with unsteady phenomena. Figure 12 shows the

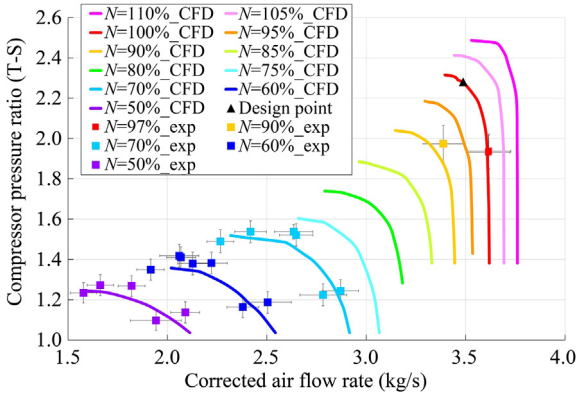

Figure 10 Compressor characteristic map for mixed-flow compressor (total-to-static).

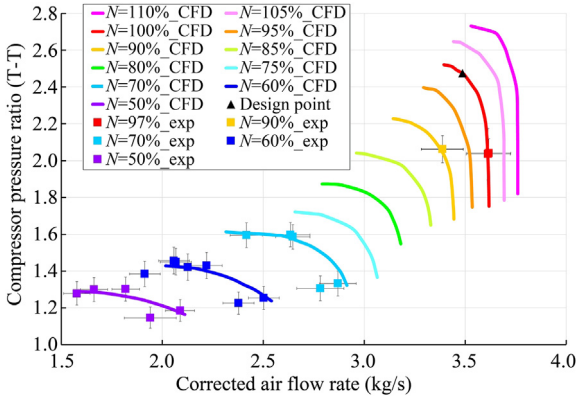

Figure 11 Compressor characteristic map for mixed-flow compressor (total-to-total).

experimental and numerical results of the adiabatic compression efficiency (total-to-static), $\eta_{s,comp}$. The error bars in Figure 12 also indicate measurement errors. The analytical results of $\eta_{s,comp}$ also have good agreements with the experimental data. From the results in Figures 10−12, the present CFD analysis can predict this mixed flow compressor performance appropriately. The discussion about the compressor operating characteristics in the subsequent section is based on those CFD results.

5.2. *Effect of ram combustion efficiency on compressor operation*

The experimental data of the mixed-flow compressor validates its numerical prediction in the preceding subsection. To analyze the GG-ATR engine performance, the authors arrange those mixed flow compressor data into the GATRECA code. The constraints of the GG-ATR engine operation are shown in Eqs. (1) and (2). The GATRACA code resolves those constraints based on the engine component performances and predicts the compressor operating state on its characteristic maps. The pressure ratio/corrected airflow rate curves of the mixed flow compressor are shown in Figure 13. The rotational speeds of those

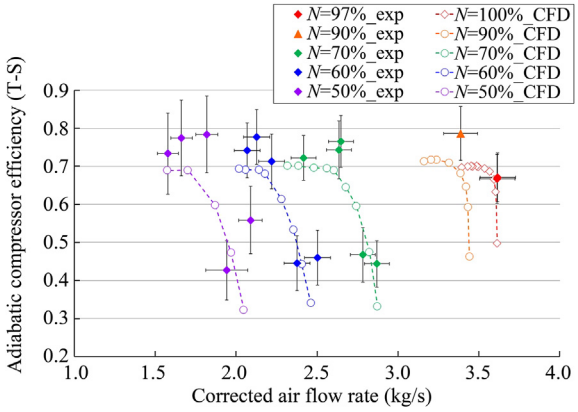

Figure 12 Adiabatic compression efficiency for mixed-flow compressor (total-to-static).

curves are the referential rotational speeds. This figure also shows the operating lines of constant ram combustion efficiency, η_{ram}. η_{ram} in Figure 13 is equal to 85%, 90%, 95%, and 100%.

Those operating lines in Figure 13 indicate the quasi-steady throttling behaviors, where the compressor power strictly equals the turbine power. The actual GG-ATR engine has dynamic throttling behaviors, where the turbine power is no longer equal to the compressor one. The dynamic throttling behaviors of a gas turbine engine are described in Refs. [30,31]. On the other hand, the dynamic throttling analysis necessitates the non-steady behaviors of a compressor and a turbine. The authors treat the transient responses in Figure 13 as quasi-steady states, and those responses have tiny throttling deviations. Figure 13 shows that a low η_{ram} reduces the compressor pressure ratio. Lowering η_{ram} decreases the ram combustor temperature, T_{T7}. As indicated in Eq. (18), the reduction of T_{T7} leads to the increase in the airflow rate, m_{air}, at the nozzle throat and the decrease in the ram combustor pressure, P_{T7}. This situation will also reduce the compressor pressure ratio π_{comp}. Therefore, lower T_{T7} shifts the compressor operation to choke side condition in the GG-ATR engine operation. A

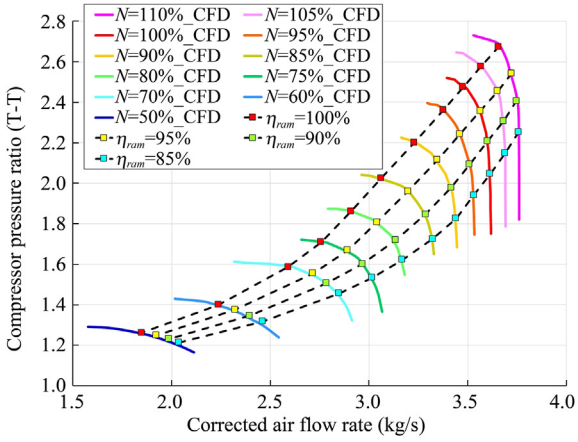

Figure 13 Operating line of constant η_{ram} efficiency.

turbojet engine with an afterburner has a variable nozzle, which changes the nozzle throat cross-sectional area with the exhaust gas temperature. However, the present GG-ATR engine uses a fixed nozzle to avoid complicated mechanical structures. The nozzle throat cross-sectional area is set based on $\eta_{ram} = 100\%$ in the current study. If the nozzle throat cross-sectional area is too small, the compressor might enter surge/stall conditions. However, it is difficult to estimate the combustion efficiency of a ram combustor. Therefore, the design of the nozzle throat must proceed by trial-and-error. This design process will be costly and time-consuming. Thus, it is reasonable to design the nozzle throat based on $\eta_{ram} = 100\%$ to avoid the risk of surge/stall.

5.3. *Throttling characteristics of GG-ATR engine*

Throttling of the GG-ATR engine requires controlling the mass flow rates of propellants, m_{GG}. The right-hand side of Eq. (1) indicates the turbine power, which drives the GG-ATR engine rotor. In Eq. (1), the mass flow rate of GG propellants can directly contribute to the turbine power. Moreover, as shown in Eq. (3), m_{GG} is proportional to the GG combustion pressure, P_{GG}. Thus, P_{GG} can be the indicator to show the throttling level.

Figure 14 shows the constant P_{GG} lines on the mixed-flow compressor characteristic map. The higher N_{cor} requires high P_{GG} in general. Figure 15 indicates the dependency of N_{cor} on η_{ram} with constant P_{GG}. Along the constant P_{GG} line, the compressor operating state shifts to low π_{comp} condition as η_{ram} decreases. This behavior indicates the same tendencies in Figure 14. In the actual GG-ATR engine throttling, N_{cor} is controlled by monitoring P_{GG}. The rotational speed becomes higher than expected for lower ram combustion efficiency. In Figure 15, on the line of $P_{GG} = 1.3$ MPa, N_{cor} is nearly equal to 100% at $\eta_{ram} = 100\%$, and N_{cor} accelerates to 107.7% when η_{ram} decreases to 82%. However, N_{cor} is 69.7% at $\eta_{ram} = 100\%$ on the line of $P_{GG} = 0.6$ MPa, while N_{cor} slightly increases to 72.3% at $\eta_{ram} = 82\%$. That means that the lower ram combustion efficiency can cause overspeeding for the GG-ATR engine. The overspeeding by degraded η_{ram} is

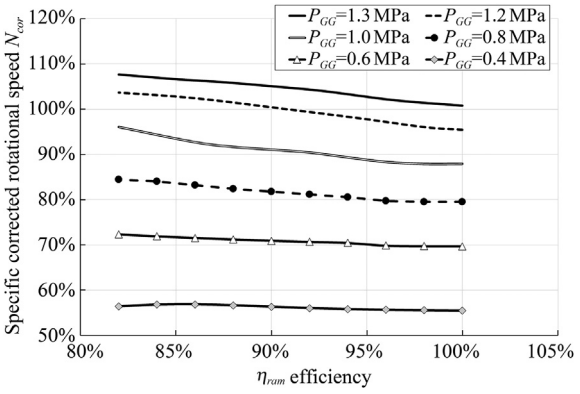

Figure 15 N_{cor}-η_{ram} efficiency correlation.

prominent for higher P_{GG}, and it is negligible in the case of low P_{GG}. The numerical and experimental compressor powers are shown in Figure 16 to explore the mechanism of this overspeeding. The error bar of the compressor power indicates measurement errors. The left-hand side of Eq. (1) corresponds to the compressor power. The experimental compressor power is evaluated by using the airflow rate and the temperature rise on the compressor as Eq. (21).

$$w_{comp} = \frac{\dot{m}_{air} C_P T_{T2}}{\eta_{comp}} \left(\pi_{comp}^{\frac{\kappa-1}{\kappa}} - 1 \right) = \dot{m}_{air} C_P (T_{T3} - T_{T2}) \tag{21}$$

Figure 17 indicates the experimental P_{GG} in the turbomachinery tests using GN_2 as the turbine driving gas. Those data are expressed as functions of m_{cor}. In Figure 16, the right side of each compressor power curve corresponds to the choke side condition. In the CFD results, the compressor powers decrease on the choked side in high N_{cor} conditions. However, the compressor power curves for N_{cor} from 50% to 70% are flat to m_{cor}. Low N_{cor} generally leads to low π_{comp}. Different from higher N_{cor}, the reduction of π_{comp} due to degraded η_{ram} is not so significant in lower N_{cor} conditions. Therefore, the variation of the compressor power is relatively small. Unfortunately, the helium gas is very costly, although it is

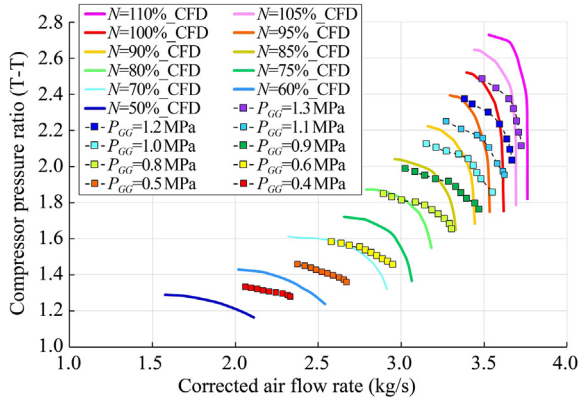

Figure 14 Constant P_{GG} lines on compressor map.

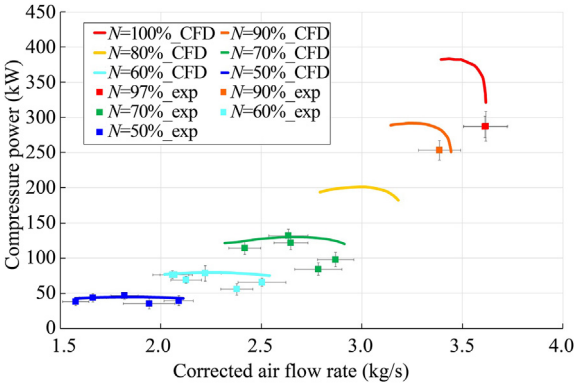

Figure 16 Numerical and experimental compressor power.

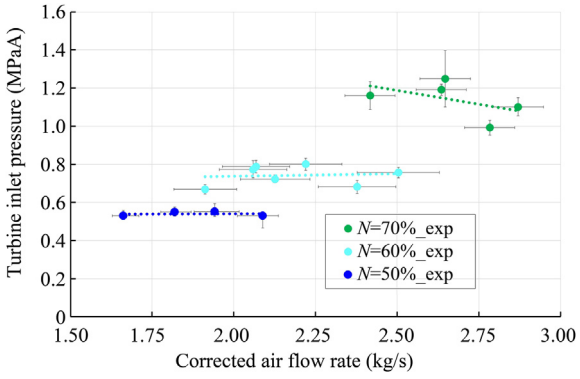

Figure 17 Experimental P_{GG} in turbomachinery test for GN_2.

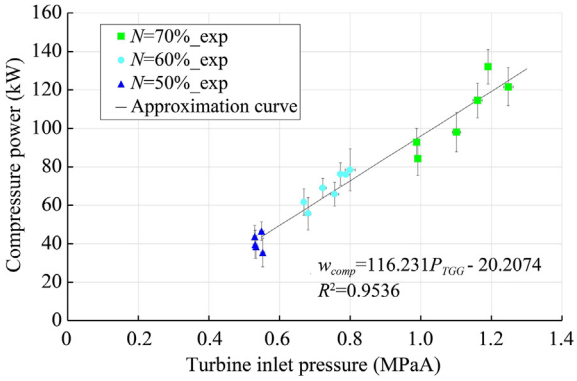

Figure 18 Correlation between P_{GG} and compressor power in turbomachinery test.

necessary for tests higher than N_{cor} = 70%. Thus, the experimental data of more than N_{cor} = 70% are limited. The experimental compressor power data for N_{cor} = 50% and 60% agree with the CFD results well. Those for N_{cor} = 70% agree with the CFD results well in the surge side condition. However, some differences between the experimental and numerical results appear in the choke side condition. The experimental compressor power for N_{cor} = 70% shows a reduction in the choke side condition. This decrease corresponds to those of the numerical results in higher N_{cor} conditions. If the compressor power becomes less in the choke side condition, the required turbine power also decreases. Those results can explain the overspeeding mechanism in lower η_{ram} conditions, as shown in Figures 14 and 15. As discussed in Subsection 5.2, Eq. (18) indicates that lower T_{T7} causes m_{cor} to increase and P_{T7} to decrease. This means that lower η_{ram} results in the compressor operation under choked conditions. The compressor power becomes lower in this situation. Therefore, in lower η_{ram} conditions, overspeeding will occur if P_{GG} keeps at the same level.

The experimental P_{GG} in Figure 17 corroborates the behaviors of compressor power in Figure 16. The pressure level of GN_2 in Figure 17 is quite different from those of GG combustion gas because the T_{GG} of GN_2 is much lower than that of GG combustion gas. P_{GG} is proportional to the mass flow rate of GN_2 as described in Eq. (3). Thus, P_{GG} can be the indicator to show the throttling level because the turbine power depends on the mass flow rate of the turbine driving gas. In Figure 17, the behaviors of P_{GG} for N_{cor} = 50% and 60% are nearly flat to m_{cor}. However, P_{GG} for N_{cor} = 70% tends to decrease with m_{cor}. This decrease in P_{GG} corresponds to the decline of the compressor power in Figure 16.

Finally, Figure 18 shows the correlation between P_{GG} and the compressor power in the turbomachinery tests using GN_2. The compressor power is linearly proportional to P_{GG}. Both the compressor power and P_{GG} become less on the choke side, as shown in Figures 16 and 17. The turbine power largely depends on the mass flow rate of GN_2 and is equal to the compressor power. P_{GG} is also linearly proportional to the mass flow rate of GN_2. The experimental results in Figures 17 and 18 corroborate the analytical results of overspeeding due to low η_{ram} in Figures 13 and 14. The ram combustor characteristics were not included in the previous study by Bossard and Thomas [11], and the potential for overspeeding was not recognized in the GG-ATR engine. However, the current GG-ATR engine cycle analysis, which takes into account the characteristics of the compressor, the turbine, and the ram combustor, indicates that overspeeding may occur. The current result suggests that the nozzle throat design requires estimating the accurate η_{ram} to keep the GG-ATR engine from overspeeding.

6. Conclusion

The authors conducted the numerical and experimental investigation of the mixed-flow compressor for the GG-ATR engine and discussed the possibility of rotor overspeeding. The conclusions of the present study are summarized below.

1. The CFD results agree well with the experimental results for the pressure ratio/the corrected airflow rate characteristics and the adiabatic compression efficiency. Using those CFD results, the authors developed the GG-ATR engine cycle analysis (GATRECA) code, including the turbomachinery, the gas generator, and the ram combustor performances. The analytical results of the GATRECA code can obtain a good agreement with CFD analysis for the mixed flow compressor performance.
2. The GATRECA analysis indicates that the compressor pressure ratio, π_{comp}, and compression power decrease for a fixed nozzle if the ram combustion efficiency decrease. The low ram combustion efficiency results in the low ram combustion temperature, which increases the airflow rate and reduces the compressor pressure ratio, π_{comp}. Low π_{comp} reduces the compressor power, and the required turbine power decreases in turn. The turbine inlet pressure does not have to be so high when the compressor operates on the choke side. As a result of the lower compressor power, this scenario leads to the overspeeding of the rotor. To avoid stall/surge conditions or overspeeding, an accurate model to predict the ram

combustion efficiency is necessary for the design of the ram combustor nozzle throat.

3. In the current experiment, the compressor power tends to be lower in the choke condition. The turbine inlet pressure is proportional to the compressor power. Those behaviors can explain that the low ram combustion efficiency could cause overspeeding for the GG-ATR engine.

The author's GG-ATR engine is being repaired to improve the reliability of its rotor-bearing system at the moment. In the future study, the authors will conduct the combustion test of this GG-ATR engine, where the GG combustion gas is employed to drive the turbine. The current results can be a valuable guideline for the GG-ATR engine operation. The authors will verify the present analytical result in the GG-ATR engine combustion test.

References

[1] K. Christensen, Air turborocket/vehicle performance comparison, J. Propul. Power 15 (5) (1999) 706−712.

[2] C.A. Snyder, A Parametric Study of a Gas-Generator Airturbo Rocket (ATR), 1986, NASA TM 88808.

[3] W.H. Heiser, D.T. Pratt, Hypersonic airbreathing propulsion, in: AIAA Educational Series, AIAA Inc., Washington DC, 1994, pp. 457−464.

[4] H. Pan, P. Zhou, Performace Analysis of Liquid Air Turborocket, in: Proceeding of the 46th AIAA Aerospace Sciences Meeting and Exhibit, Reno, NV, January 7-10, 2008, AIAA Paper 2008-70.

[5] V.F. Villace, G. Paniagua, J. Steelant, Installed performance evaluation of an air turbo-rocket expander engine, Aero. Sci. Technol. 35 (2014) 63−79.

[6] R. Minato, Advantage of ethanol fuel for gas generator cycle air turbo ramjet engine, Aero. Sci. Technol. 50 (2016) 161−172.

[7] R. Minato, Alcohol and alkane fuel performance for gas generator cycle air turbo ramjet engine, Aero. Sci. Technol. 91 (2019) 337−356.

[8] R. Minato, Low toxic nitromethane based monopropellant for gas generator cycle air turbo ramjet engine, Propulsion and Power Research 11 (3) (2022) 311−324.

[9] H. Kobayashi, Y. Maru, M.P. Richardson, K. Kinefuchi, T. Sato, Conceptual design study of a vertical takeoff and landing airbreather, J. Spacecraft Rockets 58 (5) (2021) 1279−1292.

[10] K. Mizobata, R. Minato, K. Higuchi, M. Ueba, S. Takagi, D. Nakata, K. Higashino, N. Tanatsugu, Development of a small-scale supersonic flight experiment vehicle as a flying test bed for future space transportation research, in: ISTS Special Issue: transactions of JSASS, Aerospace Technology Japan, 12, No. ISTS 29, 2014, pp. Po 3 1−Po3 10.

[11] Y. Sato, R. Imai, D. Nakata, R. Minato, M. Uchiumi, Study on propellant supply system for small-scale supersonic flight experiment vehicle (development of design technology for LOX supply system), Int. J. Microgravity Sci. Appl. 37 (1) (2020) 370104.1−370104.7.

[12] K. Arimatsu, D. Nakata, R. Minato, I. Yoshikawa, H. Yagihashi, M. Uchiumi, On the pressure loss characteristics of liquid oxygen considering a heat input, Trans. JSASS Aerospace Technol. Jpn. 19 (2) (2021) 217−223.

[13] J. Li, K. Liu, Y. Gao, S. Liu, W. Wang, Y. Liu, Combustion characteristics experimental study of solid hydrocarbon propellant for air turbo rocket, J. Propul. Power 34 (5) (2018) 1198−1205.

[14] S. Liu, J. Li, G. Zhu, W. Wang, Y. Liu, Mixing and combustion enhancement of turbocharged solid propellant ramjet, Acta Astronaut. 143 (2018) 193−202.

[15] J. Li, K. Liu, Y. Liu, S. Liu, Concept and performance study of turbocharged solid propellant ramjet, Acta Astronaut. 147 (2018) 431−444.

[16] J.S. Lilly, S.E. Hecht, B.G. Kirkham, C.A. Eadon, Experimental evaluation of an air turbo ramjet, in: Proceeding of the 30th AIAA/ASME/SAE/ASEE joint propulsion conference, Indianapolis, IN, June 27-29, 1994, AIAA Paper 94-3386.

[17] Y. Liu, Y. Gao, X. Pu, J. Li, G.Q. He, Operation matching model and analysis between an air inlet and a compressor in an air turbo rocket, Aero. Sci. Technol. 81 (2018) 306−315.

[18] G. Bussi, G. Colasurdo, D. Pastrone, Analysis of air-turborocket performance, J. Propul. Power 11 (5) (1995) 950−954.

[19] M.E. Thomas, Monorotor turbomachinery for air-turbo-rocket propulsion, in: Proceedings of the 31th AIAA/ASME/SAE/ASEE Joint Propulsion Conference and Exhibit San Diego CA, July 10-12, 1995, AIAA Paper 95-2804.

[20] J.A. Bossard, M.E. Thomas, The influence of turbomachinery characteristics on air turbo rocket engine operation, in: Proceedings of the 36th AIAA/ASME/SAE/ASEE Joint Propulsion Conference and Exhibit Huntsvill AL, July 16-19, 2000, AIAA Paper 2000-3308.

[21] ISO/Technical Committees 30, Measurement of fluid flow by means of pressure differential devices inserted in circulat cross-section conduits running full — Part 2: Orifice plates, first ed., ISO 5167-2, 2003.

[22] G.C. Oates, Aerothermodynamics of gas turbine and rocket propulsion, in: AIAA Educational Series, AIAA Inc., Reston, Virginia, 1997, pp. 313−326.

[23] J.D. Mattingly, Element of propulsion, in: AIAA Educational Series, AIAA Inc., Reston, Virginia, 2006, p. 459.

[24] Liquid Rocket Engine Turbine, 1974, NASA SP-8110.

[25] K. Christensen, Comparison of methods for calculating turbine work in the air turborocket, J. Propul. Power 17 (2) (2001) 256−261.

[26] S. Gordon, B.J. McBride, Computer Program for Calculation of Complex Chemical Equilibrium Compositions and Applications, 1994, NASA RP-1311.

[27] A.H. Shapiro, The Dynamics and the Thermodynamics of Compressible Fluid Flow, The Ronald Press Company, New York, 1953, pp. 190−203.

[28] J.E. McAulay, M. Abdelwahab, Experimental Evaluation of a TF30-P-3 Turbofan Engine in an Altitude Facility: Afterburner Performance and Engine-Afterburner Operating Limits, July, 1972, NASA TN-D-6839.

[29] L.E. Snyder, G.L. Commerford, Supersonic unstalled flutter in fan rotors; analytical and experimental results, J. Eng. Power Trans. ASME Ser. A 96 (4) (1974) 379−386.

[30] B. Maclsaac, R. Langton, Gas Turbine Propulsion System, John Wiley & Sons, 2011, pp. 295−306.

[31] L.C. Jaw, J.D. Mattingliy, Aircraft engine controls design, system analysis, and health monitoring, in: AIAA Educational Series, AIAA Inc., Reston VA, 2009, pp. 37−93.